PROGRESS IN PHOTOVOLTAICS: RESEARCH AND APPLICATIONS
Prog. Photovolt: Res. Appl. 2011; **19**:97–112
Published online 11 March 2010 in Wiley Online Library (wileyonlinelibrary.com). DOI: 10.1002/pip.963

APPLICATIONS

A self-calibrating led-based solar test platform

Frederik C. Krebs*, Kristian O. Sylvester-Hvid and Mikkel Jørgensen

Risø National Laboratory for Sustainable Energy, Technical University of Denmark, Frederiksborgvej 399, DK-4000 Roskilde, Denmark

ABSTRACT

A compact platform for testing solar cells is presented. The light source comprises a multi-wavelength high-power LED (light emitting diode) array allowing the homogenous illumination of small laboratory solar cell devices (substrate size 50×25 mm) within the 390–940 nm wavelength range. The spectrum can be synthesized by independent tuning of the 18 different wavelengths to mimic AM1.5G as well as various indoor lamp spectra. The intensity can be controlled with a 2^{14}-bit accuracy and intensities up to 3 suns are possible with an approximate AM1.5G spectral distribution. For several wavelengths intensities up to 10 suns is possible, and for a few wavelengths up to 30 suns can be reached. The setup is equipped with reference diodes and an optical fibre coupling enabling calibration, monitoring and control of the light impinging on the sample. Through a computer controlled interface, it is possible to perform all the commonly employed measurements on the solar cell at very high speed without moving the sample. In particular, the LED-based illumination system provides an alternative to light-biased incident photon-to-current efficiency measurement to be performed which we demonstrate. Both top and bottom contact is possible and the atmosphere can be controlled around the sample during measurements. The setup was developed for the field of polymer and organic solar cells with particular emphasis on enabling different laboratories to perform measurements in the same manner and obtain a common basis for comparing data. The use of the platform is demonstrated using a standard P3HT:PCBM polymer solar cell but is generally applicable to any solar cell technology with a spectral response in the 390–950 nm region. Copyright © 2010 John Wiley & Sons, Ltd.

KEYWORDS

solar test platform; self-calibration; LED; IPCE; inverse IPCE

***Correspondence**

Frederik C. Krebs, Risø National Laboratory for Sustainable Energy, Technical University of Denmark, Frederiksborgvej 399, DK-4000 Roskilde, Denmark.
E-mail: frkr@risoe.dtu.dk

Received 28 May 2009; Revised 8 December 2009

1. INTRODUCTION

The characterization of solar cells using a light source other than the Sun requires careful control of the light source and thus the development of solar simulators has been subject to much attention. Traditionally, the characterization of solar cells under laboratory conditions has employed xenon arc or halogen lamps to approximate the solar spectrum under which solar cells should ideally be tested. With the increasing number of experiments deployed in the characterization and analysis of solar cells, and the sophistication of these, there is an increased demand on the functionality and flexibility of the traditional light source employed. In particular experiments demanding pulsed illumination (as in flash simulators) or intensity variations over several orders of magnitude may be intricate to perform without distorting the desired spectral distribution. Additionally, lifetime experiments with prolonged irradiation intervals (several months) are challenged by the relatively short lifetimes of traditional light sources used in solar simulators.

In the emerging field of small molecule and polymer-based solar cells aimed at consumer products and product tagging, testing under various indoor illumination conditions will be of significant importance. Because the typical energy density under indoor illumination is much smaller than that provided by the Sun, the design of solar cells for such purposes will require meticulous spectral tailoring of the light harvesting properties of solar cells to match certain illumination conditions. Given the diversity of indoor illumination, such conditions are very difficult to simulate with traditional solar simulators and illumination systems capable of spectral synthesis are called for.

By virtue of their operational principle, light emitting diodes (LEDs) are excellently suited to remedy the shortcomings of traditional solar testing lamps. LEDs

offer operational lifetimes that are at least an order of magnitude longer than conventional light sources, luminance levels comparable to halogen lamps and a spectral shape independent of the required output power and pulse pattern. Consequently, an increasing number of solar cell studies are reporting the use of LEDs as the principle radiation source [1–4]. The possibility of combining and individually controlling LEDs of different colour in a single array further allows for spectral synthesis in a highly controllable manner. Recently, Bliss *et al*. [3] reported an LED-based solar simulator allowing for steady state or pulse illumination using spectral synthesis by means of LEDs in eight colours. It showed that stable and homogeneous illumination levels (either pulsed or steady state) can be obtained for a testing area of approximately 60 mm by 60 mm in Class A or B, depending on the wavelength range considered. However, this study also showed the shortcomings inherent to all LED-based systems, i.e. the ability to synthesize the spectral distribution of solar light hinges on the number of available frequencies in the diode array. Hence, to cover wavelengths above 680 nm, and thus achieve class A or B performance, additional halogen light sources were needed as shown in Reference [3]. However, as also pointed out by the authors, the commercial demand for LEDs with new spectral properties is so strong that the currently lacking wavelength regions will gradually be filled out.

In this study we present an all LED-based solar test platform (STP) employing an array of LEDs spanning 18 different wavelengths between 390 and 940 nm. The system was designed with the focus of being simple, compact, low-cost and as user friendly as possible. The system is self-calibrating and features predefined standard sample-holder geometry and fixed lamp/reflector geometry. The latter is intended to allow for the instrument to be distributed to other laboratories in identical copies thus facilitating testing of solar cells under standardized conditions in different locations and by different research teams.

In terms of the illumination system, the test platform presented is somewhat similar to the real-time quantum efficiency (RTQE) measurement system as developed by Young *et al*. [4]. Their system also employs multiple LEDs, but with wavelengths in the 300–1200 nm range, frequency modulation of each wavelength and subsequent Fourier analysis of the IV response of the solar cell. Here, however, we use constant illumination to simplify data analysis, but took great effort in designing the lamp to ensure high intensities and homogeneity of the illumination.

As the field of organic and polymer solar cells is maturing, it is becoming increasingly important that device characterization and efficiency reporting adheres to some minimum standards. This has so far not been the case and many reports on the power conversion efficiency (η) or the incident photon-to-current efficiency (IPCE) simply can not be compared because there is too great an uncertainty associated with the light sources involved. This has led to disputes over the validity of reported efficiency data [5–8] and to some extent to the idea that extensive device characteristics (such as the short circuit current) may be subject to manipulation. The best solution so far has been to obtain a certified efficiency measurement performed under simulated solar radiation from one of the few laboratories that provide solar cell verification and certification (NREL, Frauenhofer ISE, AIST, JIST). While this has lifted the ambiguity in terms of conversion efficiency in a limited number of cases, it does not address the general problem in the majority of published data.

The STP presented here conveniently meets the challenges raised above mainly due to a nonconfigurable hardware geometry, and a software suite providing various data acquisition routines. One of these we here term *inverse* IPCE as originally suggested by Cárabe [9,10] as the proper way of measuring IPCE but not reduced to practice by Cárabe. It should be seen as an improvement to performing light-biased/soaked IPCE measurements and contrary to these, it operates with a single wavelength band (fully or partially) being removed from the white light (biasing/soaking) illumination. With an LED-based light source employing a range of (nearly) monochromatic sources, such a measurement becomes practically realizable. This along with other types of acquisition routines made possible with the presented STP opens up for a wealth of new experiments.

We report the technical description of the test platform which demonstrate the optical performance of the system. We further present results from a measurement series on standard P3HT:PCBM-based polymer solar cells. These results illustrate the different types of measurements that are possible with the STP and the feasibility with which these can be performed. We finally discuss the strengths and weaknesses of the instrument in terms of these measurements.

2. TECHNICAL DESCRIPTION

2.1 Light source

The LED array has 18 different emission wavelengths which more or less represents the available high intensity single colour LEDs within the Vis-NIR range at the time of the construction of the instrument. Because the size of the LED array must match the dimensions of the solar cell substrate chosen (to simplify the optics), the array was laid out as parallel lines. For some of the weakly emitting LEDs two lines were included and we refer to the line or lines as segments). Each line consists of seven series connected LEDs with the same emission wavelength. Due to spatial limitations some segments could not be doubled and accordingly these were positioned close to the centre of the array to minimize the asymmetry in the resulting illumination pattern. The complete LED arrangement has dimensions of $47 \times 17\,\text{mm}^2$ and embodies altogether 26 LED segments with 18 wavelengths (182 individual LED chips). The distance from the LED array to the solar

Prog. Photovolt: Res. Appl. 2011; **19**:97–112 © 2010 John Wiley & Sons, Ltd.
DOI: 10.1002/pip

cell substrate is fixed at 55 mm. The total optical output of the array at the maximum current rating was 11.6 W, however, the use of efficient cooling of the array allows for a continuous optical output of up to 20 W. When operated in pulsed mode much higher optical outputs are possible.

2.2 Sample holder geometry and interconnects

The sample holder is shown in Figure 1 in its loading position. It consists of a base and an upper part (labelled 1, 2 and 3) which serves to position and contact the solar cell substrate. The base part (1), as shown schematically in Figure 2A, is mounted directly on the instrument housing and has a milled cavity centred between two rows of four spring-loaded gold contacts. The substrates must be rigid and can hold a thickness between 0.7 and 1.0 mm and dimensions of 25 mm by 50 mm (0.25 mm tolerances). The top part of the sample holder (2) is mounted on the reflector enclosure (3) which again serves as support for the LED array and its cooling fan. The whole arrangement can be displaced, vertically guided by four rods. The actual measurement is performed with the sample holder in the closed position, i.e. where the upper part (2 and 3) has been displaced down to touch the sample holder base (1). This ensures that solar cell characterization is always performed in the same fixed and standardized lamp geometry.

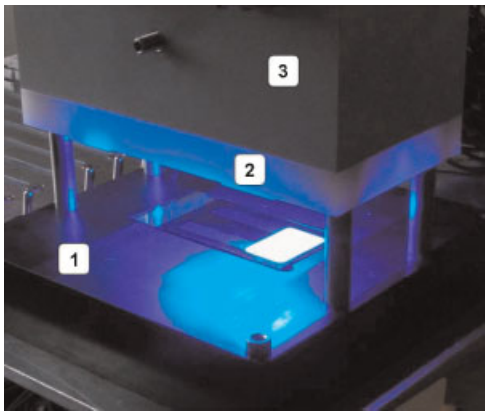

Figure 1. A photograph of the illumination and sample holder system with the 465 nm LED segment turned on and a solar cell substrate mounted. (1) Indicates the sample holder base, (2) the upper contacting structure and (3) the reflector enclosure.

The top part (2) has a similar number of contact probes as the base (1), at the same positions as in the bases (1) and a 36 mm by 26 mm aperture through which the substrate is illuminated (Figure 2B). Hence, the complete sample holder configuration provides the possibility to characterize both normal, inverted [11] and wrap-through [12] geometry solar cells with great flexibility in substrate layout. For normal geometry cells, i.e. by illumination through the substrate, measurements with full atmosphere control can be performed by virtue of the cavity fitted with a rubber gasket and gas in- and outlet in the sample holder base. The testing area is limited by the periphery of the rubber gasket and amounts to 19 mm by 27 mm (Figure 2A). For inverted geometry solar cells measurements under a protected atmosphere (only ambient pressure) can be performed by virtue of gas inlets in the top of the reflector enclosure. For calibration purposes two reference photo diodes (Hamamatsu S1133 and S5971) and an optical probe are embedded in the sample holder base as shown in Figure 2A. To allow for continuous monitoring of the illumination intensity

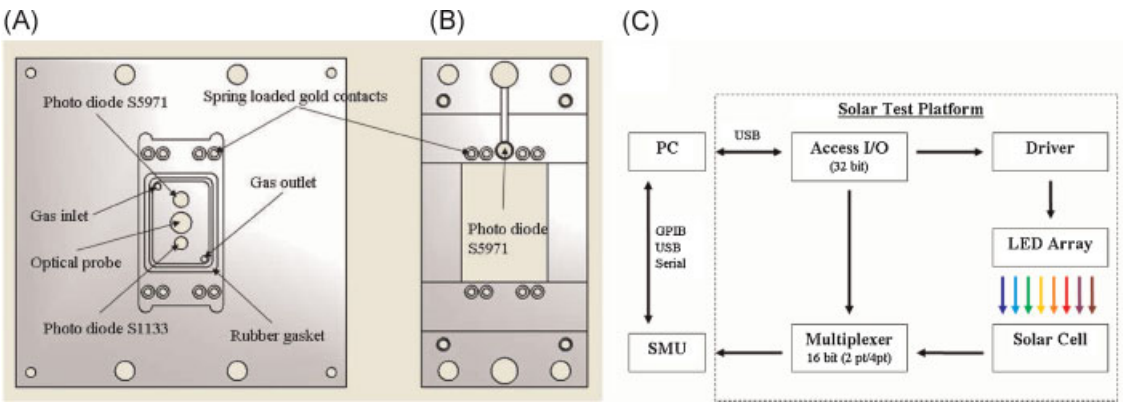

Figure 2. Shown in (A) is a schematic drawing of the sample holder base as seen from above (facing the substrate). The position of the spring-loaded contact probes, the S5971 and S1133 photo-diodes, the optical probe and the gas in- and outlet are indicated. (B) Schematic drawing of the top part of the sample holder as seen from below (facing the substrate). The position of the spring loaded contact probes and the S5971 photo-diode are shown. The illumination incident on the solar cell substrate enters through the square aperture of 26 mm by 36 mm. (C) A schematic drawing of the different components of solar test platform. The system requires only few external components (PC and SMU) and is otherwise self-contained.

during measurements, an additional reference photo diode (Hamamatsu S5971) is placed in the top part of the sample holder facing the diode array as indicated in Figure 2B.

2.3 System control and electronics

The system is outlined schematically in Figure 2C and has as external components a PC and a source meter unit (SMU). The only connections required to the system is a USB cable for communication with the PC, a power cable (85–265 VAC allowing for worldwide operation), optional gas in/outlets and an optical fibre SMA coupling for spectral analysis. The communication with the PC is via a USB2 compatible interface to a 32-bit I/O access (USB-DIO32) card with individually programmable bits. The system allows for independent control of up to 24 individual wavelengths using 24 programmable current sources. The current to each segment in the LED array is controlled via a 14-bit digital to analogue converter (DAC) configured as a voltage-to-current converter. The DAC employs a serial communication channel (clock and data) in conjunction with a DAC enable function. The 24 bits are thus used as DAC enable channels and 2 bits are used for clock and data. This allows for independent communication to one single DAC, to a group of DACs or all DACs.

2.4 Measurement modes

In continuous illumination mode, the instrument allows for a wealth of measurements to be performed, either at a single time point or as part of a time series. Basic current–voltage (*I–V*) characterization at variable illumination intensity and distributions is possible. Hence, the traditional dark, white-light and intensity dependent *I–V* characterization become a subset of a larger set of possible *I–V* characterization schemes. Throughout this study we simply refer to such measurements as *I–V* measurements. The classical IPCE measurement is simply performed by switching on a single wavelength at a time and varying the intensity through a certain range. Light-biased (light-soaked) IPCE measurements are realized through either of two acquisition schemes: in the first, a certain bias intensity distribution is specified (e.g. AM1.5G) and then the intensity of each wavelength in turn is varied e.g. as ±5, ±10, ±15, ±20%, etc., around the intensity with which it contributes to the bias distribution. In the second scheme, variation of the intensity is performed with respect to the maximum output for the given wavelength. Through these schemes, the inverse IPCE measurement also becomes possible, i.e. where one wavelength from the bias illumination is partially or entirely extinguished. Note that these acquisition schemes described specifically for the measurement of I_{sc} can be generalized to the measurement of the entire *IV*-curves, which however is outside the scope of the present study.

The possibility of performing a time series of the measurements described in conjunction with atmosphere control and temperature monitoring is very convenient for life-time and degradation studies [13]. Finally, it should be noted that all types of measurements outlined above are also possible by operating the instrument in pulsed illumination mode. However, here we demonstrate the continuous illumination mode only.

3. OPTICAL PERFORMANCE

3.1 Spectral synthesis

Spectral synthesis is achieved by selectively controlling the intensity of LED segments with given emission wavelengths. In Figure 3 we show the spectral irradiance measured for individual wavelengths when set to 50% of full power.

The irradiance is measured in the plane of, and centred relative to, the solar cell substrate using an intensity calibrated spectrometer (AvaSpec-2048) with a cosine corrector. It should be noted that full power is not defined by the nominal power specifications as listed in Table I, but rather by the power rating determined by the electronic sub-system in the instrument. Hence, some LED segments may in fact be operated above the nominal specifications as set by the LED suppliers. Also shown in Figure 3 is the AM1.5G (ASTM standard G173 and IEC standard 60904–3 edition 2) [14] solar irradiance spectrum to provide a first glance of which intensities can be achieved within the different wavelength regions. The intensities for individual LED wavelengths as obtained by integration of the

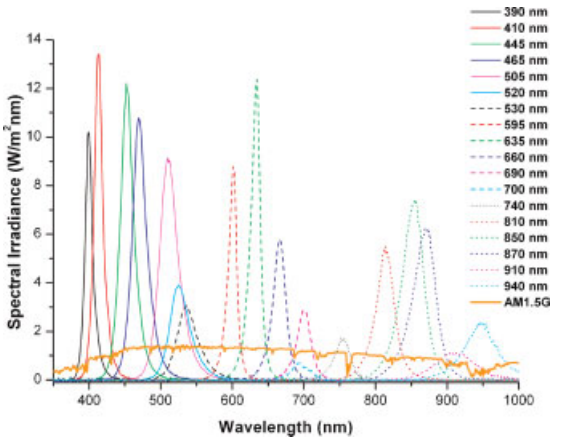

Figure 3. Spectral irradiances for individual LED wavelengths operating at a power rating of 50% as measured in the plane of and centred relative to the solar cell substrate.

Table I. Intensities as measured for the individual LED segments at 50% power rating with or without the reflector housing in the plane of and centred relative to the solar cell substrate. Also shown is the number of suns such intensities would correspond to if comparing the irradiance at λ_{peak} with the corresponding value in the AM1.5G solar spectrum. λ_{peak} and FWHM values as listed in parentheses were determined by fitting the measured irradiance spectrum for each LED segment to a Lorentz distribution. The last column lists total optical output as provided by the LED manufacturer, and as specified for the nominal power ratings for the different types of diodes

λ_{peak} (nm)	FWHM (nm)	Max intensity (W/m^2)	Suns	Max intensity (W/m^2)	Suns	Total output (mW)
		With reflector		No reflector		
390 (395)	20 (10)	147	16.2	14	1.54	700
410 (414)	20 (12)	209	14.1	24	1.62	840
445 (452)	20 (18)	295	8.99	28	0.85	1050
465 (471)	20 (23)	295	7.79	29	0.77	1050
505 (512)	25 (28)	314	6.26	29	0.58	1050
520 (528)	25 (30)	130	2.83	19	0.41	525
530 (537)	30 (30)	106	2.22	14	0.29	525
595 (601)	20 (11)	146	6.29	11	0.47	1050
635 (636)	20 (13)	233	14.51	22	1.37	1050
660 (667)	20 (19)	150	4.35	21	0.69	1050
690 (700)	22 (20)	85	2.45	12	0.35	420
700 (696)	40 (29)	22	0.60	12	0.33	168
740 (756)	35 (21)	52	1.31	10	0.25	168
810 (817)	30 (27)	181	4.87	14	0.38	560
850 (854)	50 (29)	287	6.53	20	0.46	392
870 (870)	45 (34)	253	4.74	18	0.34	700
910 (911)	60 (52)	95	1.51	4	0.06	154
940 (947)	45 (45)	141	4.54	5	0.16	154

corresponding spectral irradiances are given in Table I where they can be compared with the corresponding intensities as measured for the bare diode array, i.e. with the reflector enclosure un-mounted.

From Figure 3 it is clearly seen that in order to synthesize the AM1.5G solar spectrum the LED segments are generally operated at a power rating well below 50%. In Table I we further list how many suns the peak irradiance of each LED segment approximately corresponds to at 50% power rating, with and without the reflector enclosure mounted. We note that the two sets of peak wavelengths (λ_{peak}) and full width half maximum (FWHM) values are given in Table I. Those in parenthesis were determined by fitting the irradiance spectra to a Lorentz distribution function whereas the others are the values as provided by the vendor of the LEDs. Fitting the spectral irradiances of individual LED segments to a simple symmetric Lorentz distribution function is convenient for the purpose of determining λ_{peak} and FWHM values. However, we found that representing the spectral irradiances of the different LED segments in software as Lorentz distributions is intractable for two reasons: firstly, the spectral irradiances display a more step descent at the peak base than the corresponding Lorentz distribution (the Lorentz distribution overestimates the intensity of a LED segment). Secondly, λ_{peak} at the maximum power setting shifts for some segments and the peak become more asymmetric. This tendency is also clearly seen from Figure 4A where irradiance spectra recorded for a situation with all LED segments operating simultaneously on either 10, 20, 50, 80 and 100% rating are shown. It is seen that the shift in λ_{peak} with increasing power rating generally is more pronounced for the infra-red region. Another effect that occurs with increasing power rating is that the emission properties of a certain LED segment are influenced by the operational state of the others. This effect is shown in Figure 4B–D, where the spectra for all LED segments operating simultaneously and the sum spectrum of the individual LED segments are compared for a rating of 100, 50 and 10%, respectively. For 100% rating it is obvious that the spectrum for the case of all LED segments operating simultaneously can not correctly be represented as a sum of the individual LED spectra as seen from Figure 4B. Mainly, the intensity of a certain LED segment is diminished when others are operating simultaneously, and for the infra-red region the λ_{peak} is shifted to longer wavelengths. While these effects should be borne in mind it should also be stressed that they are observed at very high power ratings close to 100% (Figure 4B) and only to a slight extent above 50% (Figure 4C). They are not observed at the power ratings employed when simulating around 1 sun (ca. 10%

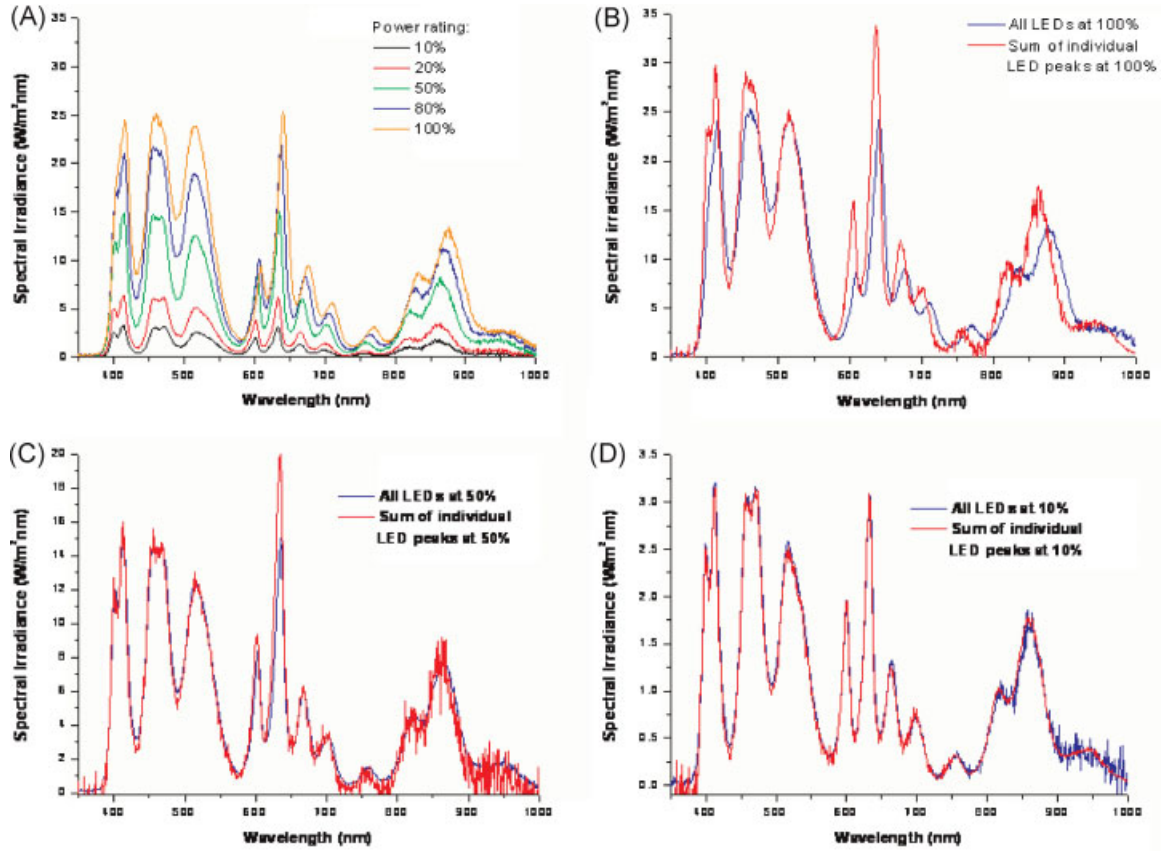

Figure 4. Spectral irradiances for the LED array operating at different power ratings. In (A) the spectral irradiance spectra are shown for all LED powered on at 10, 20, 50, 80 and 100% rating. In (B), (C) and (D) the spectral irradiance for all LED powered on simultaneously are compared with sum spectra for a power rating of 100, 50 and 10%, respectively.

power rating, Figure 4D). By virtue of the multiple power supplies supplying the diode array, we attribute these effects at high power ratings to thermal effects within the diode array.

Figure 5 shows the synthesis of the AM1.5G solar irradiance distribution by having an integrated intensity of ~700 W/m^2 between 350 and 1000 nm. The corresponding power ratings employed in the spectral synthesis and the number of suns it would correspond to are shown in Table II. To obtain a better coverage of some of the voids in the resulting spectrum, our final AM1.5G synthesis integrates to 743 W/m^2. For comparisons, the AM1.5G and the lamp spectrum for the Xe-lamp used below for some of the solar cell measurements are also shown in Figure 5. Clearly, the AM1.5G synthesis in Figure 5 suffers from the lack of several wavelengths in order to provide a balanced AM1.5G synthesis.

In particular the wavelengths around 470, 570, 740 and 770 nm are missing whereas in the infra-red the AM1.5G distribution is synthesized fairly well. The ability to spectrally synthesize this region is illustrated

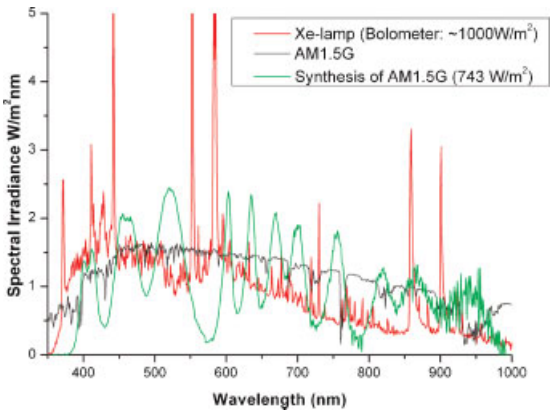

Figure 5. Spectral synthesis of the AM1.5G spectrum as obtained with the LED array in the solar test platform. For comparisons are shown the AM1.5G spectrum and the lamp spectrum for the Xe-lamp also employed in this study. The spectral synthesis has been performed such that the intensity integrates to 743 W/m^2 for the wavelength interval 350–1000 nm.

Table II. Relative power ratings required for each LED wavelength to synthesize the AM1.5G distribution and the intensity distribution of a 20 W halogen lamp. Also shown are the equivalent number suns these ratings correspond to within the FWHM of each LED wavelength

λ_{peak} (nm)	Power rating (%)	Suns	Power rating (%)	Suns
	AM1.5G		20 W Halogen	
390	6	1.95	0	0
410	5	1.41	0	0
445	7	1.26	0	0
465	7	1.09	0.2	0.03
505	7	0.88	0	0
520	15	0.85	0	0
530	13	0.58	2	0.09
595	14	1.76	1.5	0.19
635	6	1.74	0.5	0.14
660	17	1.48	3	0.26
690	27	1.32	3	0.16
700	28	0.34	19	0.22
740	62	1.62	18	0.47
810	15	1.46	7	0.55
850	6	0.78	1	0.12
870	8	0.76	5.2	0.49
910	29	0.88	16	0.52
940	30	2.72	18	1.29

in Figure 6, where the synthesis of the irradiance spectrum of a 20 W halogen (M16 with parabolic reflector) at 20 cm distance is shown. Here the synthesis has been performed such that an intensity of 192 W/m^2 was matched between 350 and 1000 nm. The required power ratings for each LED segment are listed in Table II.

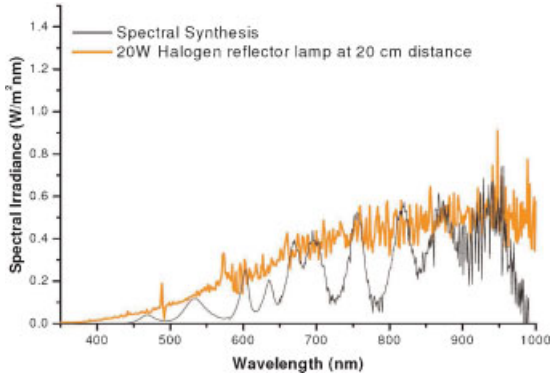

Figure 6. Spectral synthesis of the irradiance distribution from a 20 W halogen lamp using the diode array. The synthesis has been performed such that the intensity integrates to 192 W/m^2 for the wavelength interval 350–1000 nm.

3.2 Homogeneity

The homogeneity of the illumination from the diode array was determined by mapping the illumination intensity in the *XY*-plane corresponding to the position of the solar cell substrate. The mapping was done using a Hamamatsu S5971 photo-diode mounted on an *XY*-scanning stage with sub-millimetre resolution. The mapping resolution was determined by the active area of the photo-diode and corresponded to a spot size of 1.2 mm in diameter. In Figure 7 we show the intensity maps obtained for individual LED segments when operating them at approximately 50% power rating. The different contour colours correspond to a bin size of 25 W/m^2. The fact that some LED segments physically are represented by only one diode string is clearly seen from the intensity maps in Figure 7. Hence, the 390, 410 and 530 nm maps display intensity variations of up to 50 W/m^2 over an area corresponding to the largest active area possible on the solar cell substrate. This active area is shown with a blue frame on each of the maps in Figure 7 and is 27 mm by 19 mm.

Within this area the 445, 465 and 520 nm maps in principle display a variation up to 75 W/m^2, which for practical purposes can be limited to 50 W/m^2 by restricting the active area in the *X*-direction. For the remaining wavelengths, maximal intensity variations range between 25 and 50 W/m^2 over the active area, these being mainly due to the limited LED array dimension in the *Y*-direction. A more detailed view of the intensity variation of the data in Figure 7 is shown in Figure 8 where the intensity along the $Y=0$ line is plotted. Apart from the LED segments with wavelengths 410, 445, 465, 520 and 530 nm, the intensity is homogeneous to within $\sim$10 W/m^2 along the line $Y=0$, in the plane of the solar cell substrate. In terms of I_{sc} we may summarize the effect of the lamp in-homogeneity by integrating the measured S5971 current densities over the 19 mm by 27 mm area (in Figure 7). This is then compared with the current obtained if using the highest current density within this area. In the worst case, i.e. for the 520 nm LED segment, the variation in I_{sc} amounts to $\sim$4%. For LED segments with spatial intensity variation below 10 W/m^2 the corresponding variation in I_{sc} is below 2%.

3.3 Instrument self-calibration

The instrument is self-calibrating and the calibration procedure must be performed with an empty and closed sample holder at instrument start-up. The procedure relies on an instrument specific correlation between the spectral irradiance of the individual LED segments as measured with an optical probe, and the current response from the S5971 and S1133 photo-diodes. The calibration is performed for individual LED segments in turn, varying the intensity through the possible 2^{14} settings in

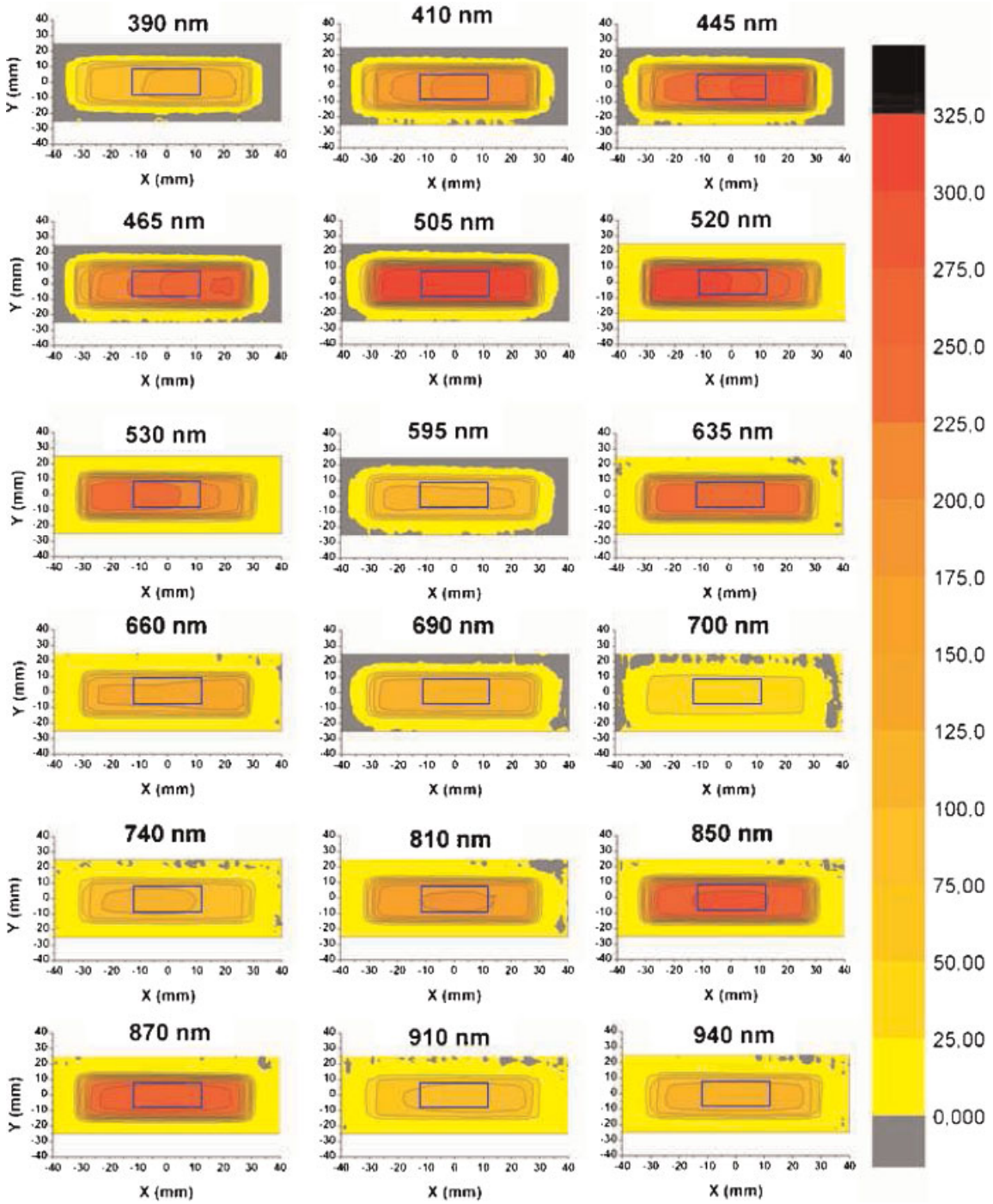

Figure 7. Mapping of the illumination intensity in W/m^2 of the diode array with individual LED segments operating at a power rating of approximately 50%. The mapping was performed with a resolution corresponding to a spot of 1.2 mm. The largest active area possible for solar cells is shown with a blue frame and amounts to 27 mm by 19 mm.

256-bit steps, i.e. 128 steps for each LED wavelength. The short circuit current from the S5971 photo-diode is measured at each point and stored together with the corresponding 14-bit representation of the power settings in a lookup table. From the photo-response characteristics of the S5971 photo-diode [15], a correlation between the instrument specific power ratings and the intensity of the LED segment is thus obtained as a

Prog. Photovolt: Res. Appl. 2011; **19**:97–112 © 2010 John Wiley & Sons, Ltd.
DOI: 10.1002/pip

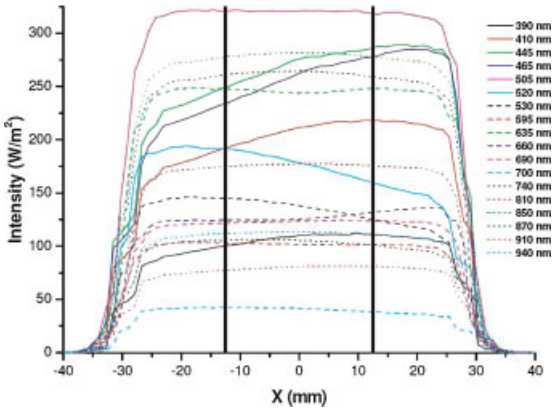

Figure 8. Mapping of the illumination intensity in W/m^2 along $Y = 0$ for the diode array with individual LED segments operating approximately at a power rating of 50%. The mapping was performed with resolution corresponding to a spot size of diameter 1.2 mm. The width of the largest active area possible for solar cells is shown with vertical black lines.

lookup table for each wavelength. We found a nonlinear relationship between the 14-bit power setting and the measured current from the photo diode: the LED segments require a certain onset value, followed by an almost linear regime and ending in a saturated regime near full rating. When a given power rating is requested for an LED segment, the nearest values in the lookup table is found and linear interpolation is used to calculate the 14-bit value being sent to the access I/O board.

This procedure also serves to linearize the relationship between the relative LED rating and the irradiance measured.

4. APPLICATION EXAMPLE: P3HT:PCBM SOLAR CELLS

To illustrate the versatility of the instrument, in the following we display measurement results obtained for a series of five devices (labelled 1 to 5), each with four solar cells on them. The solar cells were built using the well-known P3HT:PCBM photo-active blend in the device configuration: Glass | ITO | PEDOT:PSS | P3HT:PCBM | Al. The measurements were conducted consecutively for the five devices starting at noon on a sunny day which allowed for outdoor characterization on a solar tracker system as well. The solar cells were kept in a glove box environment for 5 min before the measurement starts. In Table III, we summarize the characterization steps performed for each of the four solar cells on device 1 to 5, along with the approximate duration of the different data acquisition steps.

In total, characterization of a single device took about 30 min but the majority of this time was spent on mounting and un-mounting the device in different instrument setups. Hence, the actual measurement time used in the test platform amounts to less than 15 min, per device.

4.1 IV characterization under one-sun illumination

In a scatter plot representation, Figure 9A gives an overview of the current densities and efficiencies obtained for all the 19 solar cells (cell 4 on device 5 was nonfunctional) under different one-sun illuminations. These measurements include an initial and a final (1 and 8 in Table III) *I–V* scan used to quantify the extent of device degradation during the 30 min data acquisition period. The solar cell numbering (for a given device) is indicated with different symbols whereas (for sake of clarity) the device numbering is not displayed (Figure 9A). It is seen that outdoor measurements on average give $J_{sc} \sim 2$ mA/cm^2 larger than obtained with the STP. This difference may in fact be $\sim$0.5 mA/cm^2 larger when taking into account that the outdoor measurements were made just before the final measurements on the STP, which on average displayed J_{sc}, reduced by 0.5 mA/cm^2. The illumination intensity on the solar tracker was monitored bolometrically, and intensities between 983 and 998 W/m^2 were recorded during the *I–V* characterization of the five devices. The corresponding current densities shown in Figure 9A were normalized to 1000 W/m^2. Under the

Table III. Measurement types performed for each of the four P3HT:PCBM solar cells on device 1 to 5 along with the duration of the measurement time per device

Measurement/instrument	Data acquisition task	Duration (min)
1: Test platform	*I–V* scan at AM1.5G approximation (743 W/m^2)	<1
2: Steuernagel	*I–V* scan at AM1.5G approximation (bolometer: 1000 W/m^2)	<1
3: Solar Tracker	*I–V* scan under the Sun (bolometer: 982–993 W/m^2)	<1
4: Test platform	Intensity dependent *I–V* up to three time AM1.5G	~5
5: Test platform	Normal IPCE with peak intensities corresponding to AM1.5G	<1
6: Test platform	Normal IPCE with peak intensities up to 300 W/m^2	2
7: Test platform	General IPCE with a approximate AM1.5G as bias	~3
8: Test platform	IV scan at AM1.5G approximation (743 W/m^2)	<1

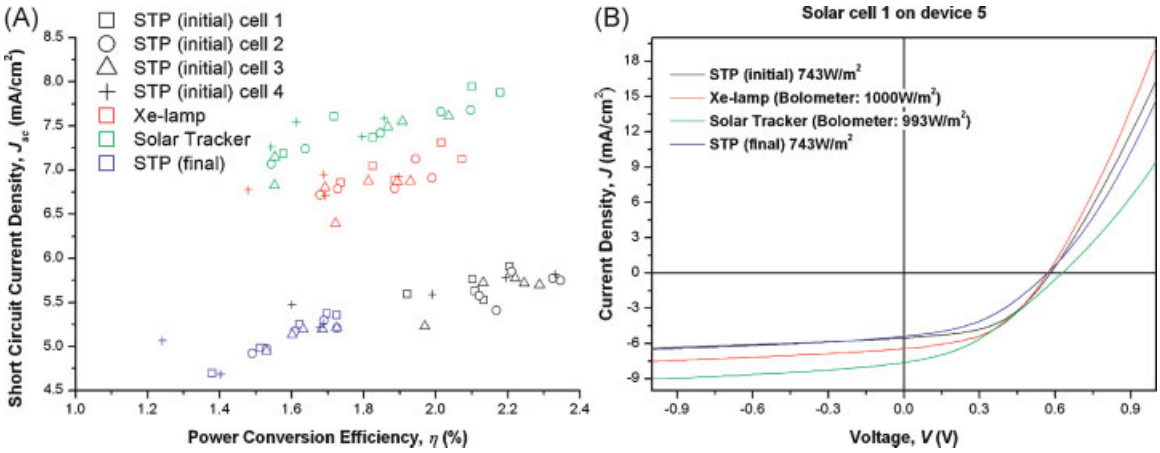

Figure 9. (A) Scatter plot showing J_{sc} versus η for all 19 solar cells on device 1 to 5 measured under different white light conditions (encoded with different colours). Different symbols designate the index of the solar cell on the device. The current density data obtained on the solar tracker has been normalized to 1000 W/m^2. (B) *J–V* curves for solar cell 1 on device 5 measured under different white light conditions.

Xe-lamp (Steuernagel Lichttechnik, calibrated bolometrically to 1000 W/m^2 using a CM4 high temperature pyranometer from Kipp & Zonen) on average J_{sc} was ~1 mA/cm^2 higher than with the STP.

As also seen from Figure 9A, it seems that the spread in the J_{sc}, data is slightly larger on the solar tracker than under the other sources. Note that the same SMU was used for the Xe-lamp and the solar tracker, and that the influence of extension cables used for outdoor measurements was tested to be negligible. In Figure 9B is shown the *J–V* curves for solar cell 1 on device 5 as obtained under different illumination. It is seen that similar values for V_{oc} and FF are obtained with the test platform and under the Xe-lamp which reflects the general trend observed for all the solar cells (results not shown). As also seen from Figure 9B, outdoor characterization gives rise to higher V_{oc} but a slightly lower FF. This again reflects a general trend for the solar cells (results not shown). Despite the generally higher J_{sc} and V_{oc} obtained under outdoor conditions, the highest efficiencies are still obtained with the STP by virtue of generally high values of FF (results not shown).

4.2 Intensity dependent IV

The intensity dependent *I–V* measurement is the most time consuming characterization step of the tasks listed in Table III because 10 *I–V* curves were recorded for each solar cell. The highest illumination level corresponds to the AM1.5G synthesis (as used above in the one-sun characterizations) but scaled by a factor of three to yield an intensity of 2230 W/m^2. Taking this as 100%, the remaining nine illumination levels are given as 90, 80, 70, ...10%. Figure 10 displays the photovoltaic key parameters J_{sc}, V_{oc}, FF and η obtained for the solar cells plotted against the illumination intensity. Figure symbols and colour coding is as in Figure 9. Despite small variations in J_{sc}, V_{oc}, FF and η between different solar cells (both within a device and between devices), overall the key parameters show uniform and clear trends. Hence, in Figure 10A a slight sub-linear correlation between J_{sc} and illumination intensity is seen. The grey line in this plot serves as a guide to the eye and is a straight line through (0,0) and the average of J_{sc} at the two lowest intensities. Figure 10B shows that V_{oc} increases with ~90 mV on increasing the illumination intensity from 0.3 suns to approximately 3 suns. The increase in V_{oc} is most rapid at low intensities and gradually saturates with increasing intensity. Conversely, the FF features a significant decrease with increasing illumination intensity as seen from Figure 10D, and this is responsible for the corresponding linear decrease in η with illumination intensity, as seen from Figure 10C.

4.3 Normal and generalized IPCE measurements

IPCE measurement data resulting from measurements 5, 6 and 7 (Table III) are displayed in Figure 11. In measurement 5 individual wavelengths are switched on sequentially at a power rating corresponding to their contribution in the AM1.5G synthesis, i.e. as used in measurements 1 and 8. Measurement 6 is performed analogously to 5, but with the intensity of each wavelength increased stepwise as 10, 50, 100, 150, 200,. . .., 300 W/m^2. The results from measurement 5 and 6 are discussed under one heading and are referred to as classical IPCE. From Figure 11A it is seen that the measured IPCE, within the photo-active wavelength region of P3HT:PCBM, exhibits a decrease with increasing illumination intensity. With

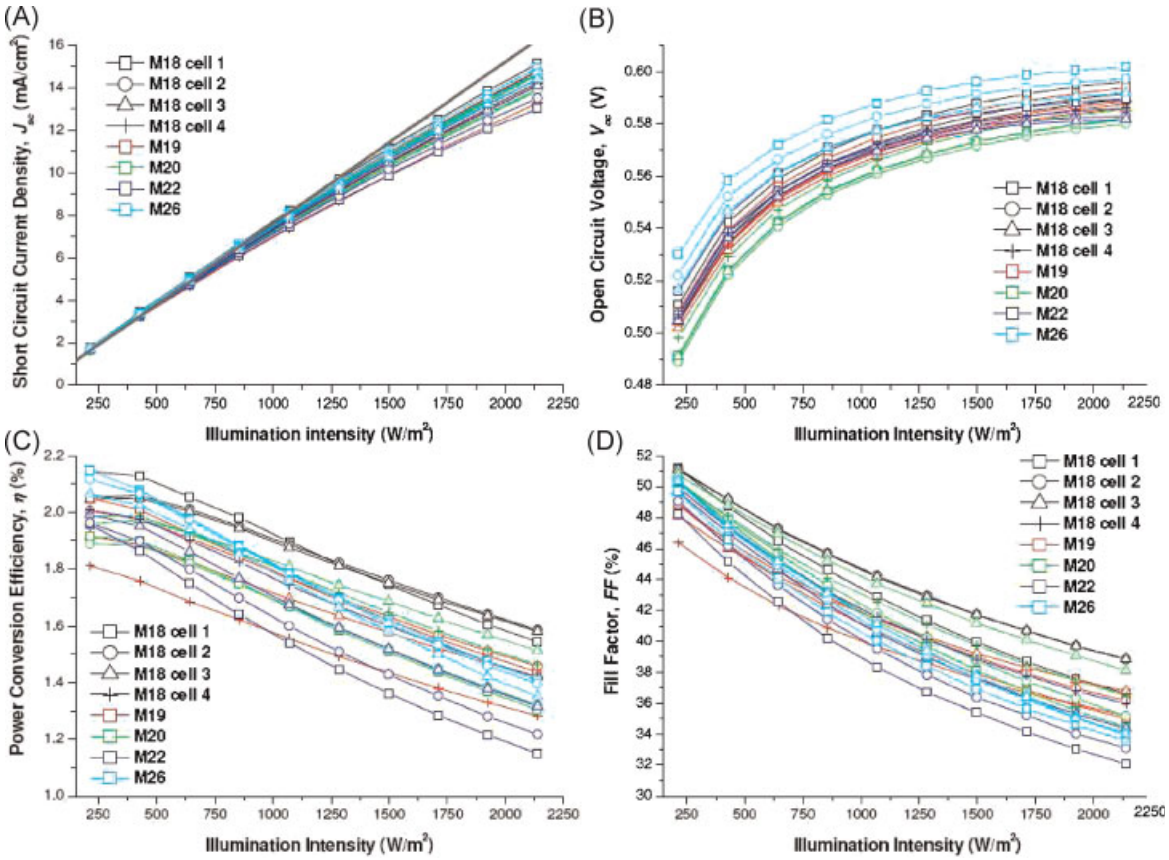

Figure 10. Key photovoltaic parameters as a function of illumination intensity as measured for the solar cells on device 1 through 5 using the solar test platform. The highest illumination level corresponds to three times the AM1.5G synthesis used for the one-sun *I–V* characterizations. The nine lower illuminations levels are given as 90, 80, 70, ...10%.

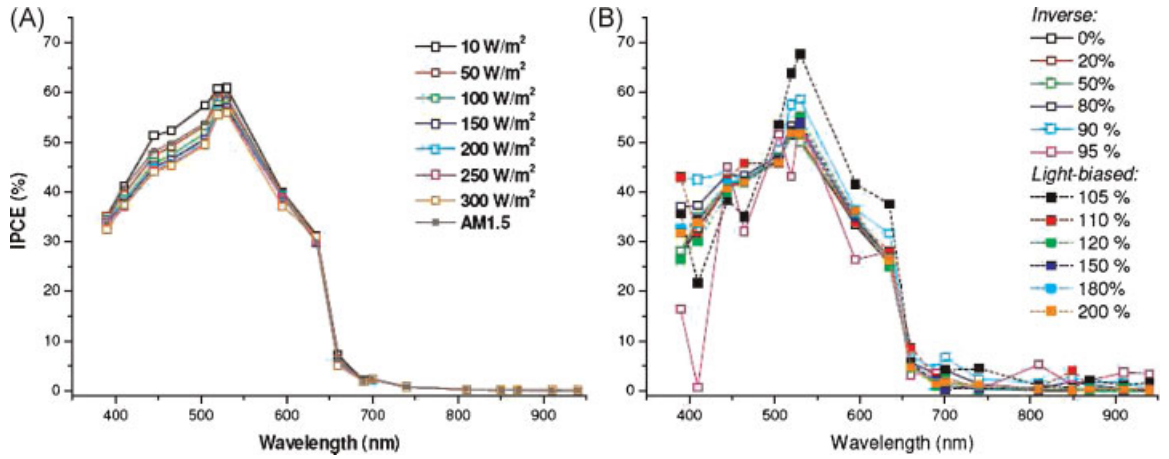

Figure 11. Different types of IPCE measurement data as measured for solar cell 1 on device 1 using the solar test platform. In (A) classical IPCE data is presented obtained with illumination intensities ranging between 10 and 300 W/m^2 for individual LED segments. In (B) general IPCE data is presented as obtained with an approximate AM1.5G bias illumination and with the irradiance for each LED wavelength varied between 0 and 200% of its corresponding AM1.5G value. Inverse IPCE measurements are shown with empty squares whereas measurements corresponding to light-biased conditions are shown with filled squares.

increasing intensity, the downward shift of the curves occurs without crossing between curves and a saturation that begins around 200 W/m^2. The IPCE curve corresponding to the AM1.5G intensities (measurement 5) does, however, cross the 10 and 50 W/m^2 curves as expected from intensities listed in Table II.

In measurement 7, the IPCE is measured using a bias illumination and varying the intensity for the individual wavelengths through a range corresponding to different fractions of their contribution to this bias illumination. As bias illumination, we use the AM1.5G synthesis. In the range where the intensity of the individual wavelengths corresponds to 0, 20, 50, 80, 90, 95% of the AM1.5G settings, inverse IPCE values are determined. Conversely, in the range where intensities are taken as 105, 110, 120, 150, 180 and 200% of the AM1.5G settings, light-biased IPCE values are determined. From Figure 11B it is seen that inverse and light-biased IPCE qualitatively display similar features, and overall a trend similar to the classical IPCE is seen. The 95 and 105% IPCE curves in Figure 11B are subject to quite some noise which is expected considering that J_{sc} values resulting from nearly equal illumination levels are subtracted in order to derive the IPCE. To facilitate a comparison of the three types of IPCE data measured for the P3HT:PCBM solar cells, in Figure 12 we display the same results as in Figure 11 but with the 95 and 105% IPCE curves omitted. For the sake of clarity no reference to the different illumination levels is given in Figure 12. It is seen that the classical IPCE values are a bit larger than general IPCE values. For the latter values, the difference between the inverse and light-biased IPCE values seems insignificant.

In terms of IPCE values, solar cell 1 on device 1 is representative of the remaining 18 solar cells which all qualitatively display the same features as shown in Figure 11. The main variation between IPCE curves for different solar cells comes from small vertical displacements of the curves reflecting the corresponding spread in J_{sc} among the solar cells (note shown).

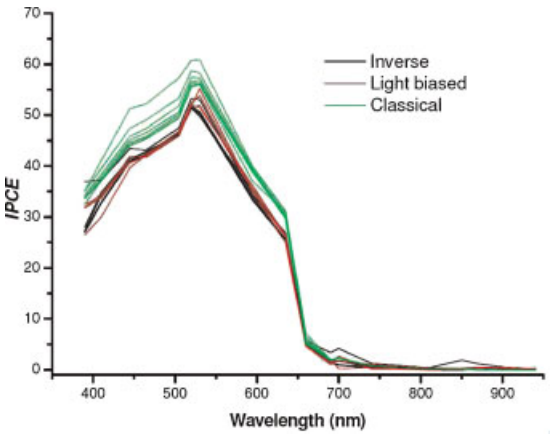

Figure 12. Comparisons of classical, inverse and light biased IPCE as measured for solar cell 1 on device 1 under different illuminations conditions. Classical IPCE curves (green) are shown for the intensities listed in Figure 11. For inverse and light-biased IPCE, results for irradiance levels listed in Figure 11 are shown except for the 95% (inverse) and 105% (light biased) curves.

5. RESULTS AND DISCUSSION

5.1 Optical performance

From the results shown in Figures 3 and 4, it is clear that for selected wavelengths irradiance levels up to 30 times that of AM1.5G can be achieved with the STP. When considering LED segments operating alone (as in Figure 4B–D) for all wavelengths, an astonishing linearity between the illumination intensity and the power rating is seen (specific results not shown). This is an asset often pointed out for LED sources and thus their use in optical measurement instrumentation. We observe that this linearity holds despite the fact that some LED segments can be operated well above their nominal power rating. However, with increasing power rating we observe a slight shift in λ_{peak} for some LED segments.

In terms of spectral synthesis of solar light, the system performs fairly balanced at intensities below 3 suns. Synthesizing higher intensities than 3 suns is not possible with the present configuration of the instrument because some LED segments simply lack the required intensity, e.g. the 700 and 740 nm segments. Also, as clearly seen from Figure 4A, the linearity ceases when multiple LEDs are operating at power ratings above ~50%. Consequently, if one were to perform intensity dependent measurements requiring a specific spectral distribution, generally one cannot simply scale the power ratings of the individual LED segments if the ratings are above 50%. In this case it would be needed to monitor the spectral distribution by means of the optical probe and make the appropriate adjustments of the power ratings. Note that the accompanying software allows the power settings of the LED array to be saved and thus a library of calibrated spectra can be built.

The general characterization purpose of the STP implies compromises in terms of accuracy for the different measurements. In practice this translates to how the diode array is laid out. Firstly, to maintain an acceptable level of homogeneity of the illumination over the device testing area, a limited number of different LED segments should be used. This is where the use of a reflecting enclosure becomes important. In the present case, the increase in the illumination intensity and the homogeneity of its spatial distribution by virtue of the enclosure is quite significant, as also partially indicated by Table I.

For spectral synthesis of various broadband light sources, a limited number of LED wavelengths are acceptable if they are chosen appropriately. Hence, neighbouring LED segments with comparable FWHM

should have a peak separation, $\Delta\lambda_{peak}$, larger than half the FWHM value, for both peaks to be useful in the spectral synthesis of broad distributions. If they lie farther apart, voids in the synthesis will appear as is the case for the AM1.5G synthesis shown in Figure 5. Conversely, if the neighbouring LED segments have a peak separation, $\Delta\lambda_{peak}$, less than half the FWHM value, λ_{peak} for the two LED segments cannot be resolved in the synthesized spectrum and for practical purposes such segments could be omitted. This for example is the case for the neighbouring 520 and 530 nm LED segments in the diode array, which both have a FWHM of 30 nm. Overall, for the synthesis of broad spectral distributions, it obviously holds that the larger the FWHM of the composite LED segments, fewer such segments are required. From the perspective of synthesizing a light source with distinct emission lines, e.g. from fluorescence lamps, as many and as narrow bandwidth closely spaced LED segments would be required in the diode array. As much as this would increase the resolution with which IPCE measurements can be performed, it would also dramatically increase the cost and complexity of the diode array, control electronics and would introduce additional problems of the spectral homogeneity of the illuminated area.

As also pointed out by Young *et al*. [4] IPCE (or quantum efficiency) measurements within seconds rather than hours is possible when using an electronically controlled LED illumination system. Whereas in Reference [4] data acquisition is performed in parallel, and thus in less than a second; here a few seconds are needed because the acquisition is performed at constant illumination and thus sequentially. We deliberately chose not to use frequency modulation of the illumination to keep the system operation as simple as possible. With frequency modulation invoked, the operator would have to assure that time constants for the particular solar cells under investigation do not coincide with the time constants of the illumination modulation. Nonetheless, performing IPCE measurements within seconds still is a substantial improvement relative to hours as required by traditional measurement systems.

5.2 Characterization of P3HT:PCBM solar cells

The device temperature under different illumination conditions is an important issue which may influence performance comparisons under different light sources. The V_{oc} has a distinct temperature dependence and is relatively independent of other measurement conditions for the P3HT:PCBM solar cells considered [16,17]. The consistently higher V_{oc} values as measured under outdoor conditions can be accounted for by a lower device temperature (10–20°C) on the solar tracker on the day of measurement than under the Xe-lamp and the STP.

According to References [16,17], J_{sc} is almost temperature independent in the considered temperature range. Combined with the fact that the average decrease in J_{sc} due to degradation is not more than $\sim$0.5 mA/cm^2, we may infer that the different ranges of J_{sc} values (Figure 9A; as measured under different light sources) primarily reflects differences in the spectral distributions (Figure 5) of the light sources. From Figure 5 it is seen that the Xe-lamp is more intense than AM1.5G between 300 and 500 nm, but less intense from 600 nm and onwards. Hence, in the 300–500 nm range, more current is generated under the Xe-lamp than under the Sun, which is compensated by less current generation in the 600–700 nm region for the Xe-lamp. Despite a larger IPCE for P3HT:PCBM in the 300–500 nm range than from 600 nm and onwards (*vide infra*), the larger photon flux in the latter range still on average gives larger J_{sc} values under outdoor conditions. That J_{sc} values as measured on the test platform on average are $\sim$25% lower than for outdoor measurements is simply due to large voids in the LED intensity distribution as compared to AM1.5G. In particular at 575 nm the void is outspoken, which coincidently falls in the range where the IPCE has its largest values for P3HT:PCBM solar cells. Using such a standard IPCE spectrum for a P3HT:PCBM solar cell, the maximum achievable J_{sc} was calculated for the three different spectral distributions in Figure 5. This confirmed the $\sim$25% lower J_{sc} obtained for the STP relative to outdoor measurements, but on the other hand showed that the same J_{sc} should have been obtained under the Xe-lamp and under the Sun. The latter we ascribe to the difficulty in precisely measuring the spectral distribution for the Xe-lamp with its distinct and sharp lines. It should be emphasized that rigorous comparisons of the lamp characteristics of the STP with other light sources generally require the use of a reference solar cell and careful consideration of the spectral mismatch [18]. Since the STP comprise two different references diodes including the S1133 that has a similar response to P3HT:PCBM devices the approach described in reference [18] can be easily applied. The data in Figure 9 should only be considered an application example, from which a first and approximate estimate of the effect of using an LED-based illumination system can be assessed for polymer solar cells.

Intensity dependent *I–V* characterization is typically performed using a range of neutral density filters inserted in the light path to preserve the lamp spectrum rather than simply adjusting the lamp power. When intensities ranging from fractions of a sun to several suns are required, a very powerful lamp and/or concentration optics is needed, combined with the handling of many filters. Altogether, this amounts to a substantial amount of delicate instrumentation which practically requires a high maintenance level. Consequently, relatively few research groups report intensity dependent *I–V* characterization under white light conditions as part of their standard characterization suite. Its importance in terms of investigating the effect

of the real solar spectrum on the V_{oc} [19] and space-charge limited current phenomena [19–23], and thus unveil fundamental device physics is important. With an LED-based illumination system, intensity dependent *I–V* characterization can be performed within minutes, with full control of the lamp spectrum and an instrument with no moving mechanical parts. The results of the intensity dependent *I–V* measurements in Figure 10 are generally in line with what previously has been observed for P3HT:PCBM solar cells. Hence, a correlation between J_{sc} and the illumination intensity (P_{in}) obeys $J_{sc} = (P_{in})^{\alpha}$, with α being less than unity (see Reference [22,23] and references therein). The intensity dependence for V_{oc}, FF and η between 200 and 1000 W/m^2 also concurs with previous reports which, however, were limited to below 1000 W/m^2 [16,17,24].

In the above discussion we implicitly assumed a knowledge of the photo-active region for P3HT:PCBM solar cells. In fact, the IPCE, or alternatively the external quantum efficiency (EQE), has been studied for P3HT:PCBM by several groups, which however all employed the classical unbiased measurement [5,25–33]. Qualitatively, all types IPCE measurements performed in this study catch the important features as generally reported for annealed P3HT:PCBM solar cells, i.e. a peak in the spectrum around 540 nm, the abrupt decline starting at 600 nm, the shoulder starting at 630 nm and a dip somewhere between 400 and 500 nm. Since the IPCE/EQE measurement depends on extensive physical properties (i.e. lamp calibration and solar cell area), the absolute position of these spectra will always be subject to debate and controversy, in analogy with reporting of the power conversion efficiency [5]. Hence, when comparing with literature data, the main focus should be on relative features of the IPCE spectra. It is reassuring, however, that the classical IPCE measurements performed with the STP generally concur with previous reports. The corresponding IPCE values obtained using the inverse and light-biased measurement modes have been reported in the context of inorganic solar cells previously using a grating monochromator and a Fourier spectrometer [9,10]. In the context of polymer solar cells, the uses of inverse and light-biased measurement modes have, to the best of our knowledge, not been reported hitherto. Qualitatively, the inverse and light-biased IPCE measurements give similar values that are slightly lower than the corresponding classical IPCE values. This is expected for solar cells governed by a nonlinearity between J_{sc} and P_{in} (Figure 10A). In the present application example, the difference between the classical and general IPCE measurements seems small. This indicates that the efficiency limiting factors for P3HT:PCBM solar cells characterized in this study lie elsewhere than in the charge extraction process. It should be kept in mind that for other and less optimized photovoltaic polymer blend systems, the general IPCE acquisition scheme may become a strong analytical tool.

6. CONCLUSION

In this work we have demonstrated a self calibrating solar test platform (STP) with a fixed lamp geometry enabling the general characterization of small laboratory solar cells. This includes *IV*-characterization under different illumination conditions, IPCE, light-biased and the so-called inverse IPCE, as well as stability/degradation measurements under controlled atmosphere. The light source was based on an array of high-power LEDs mounted in a reflector system enabling illumination levels up to 30 suns in certain wavelength ranges. In its current implementation the system can synthesize an approximate solar spectrum (AM1.5G) with intensities up to 3 suns. The system is compact with the lamp source having a volume of less than 1000 cm^3 including the cooling fan. The system as demonstrated was integrated with control electronics, communications and metering but the light source can easily be placed remote from the controls. Integration in a glovebox environment or portable operation is possible as the system operates using a line power in the range of 85–265 VAC and a single USB2 connection to a computer. The system was developed for the field of polymer and organic solar cells and enables the characterization of both normal and inverted device geometries. Using P3HT:PCBM solar cells we demonstrated the capabilities of the instrument by performing various intensity dependent *IV* and IPCE measurements. In particular we demonstrated a new type of IPCE measurement (inverse IPCE) never previously performed on polymer-based solar cells.

ACKNOWLEDGEMENTS

This work was supported by the Danish Strategic Research Council (DSF 2104-05-0052 and 2104-07-0022). The authors thank Torben Kjær for technical assistance.

REFERENCES

1. Grischke R, Schmidt J, Albert H, Laux A, Metz A, Hilsenberg U, Gentischer J. Led flasher arrays (lfa) for an improved quality control in solar cell production lines. In *European Photovoltaic Solar Energy Conference*, 2004; Vol. 2, 2591–2594.
2. Kohraku S, Kurokawa K. A fundamental experiment for discrete-wavelength led solar simulator. *Solar Energy Materials and Solar Cells* 2006; **90**: 3365–3370.
3. Bliss M, Betts TR, Gottschalg R. An led-based photovoltaic measurement system with variable spectrum and flash speed. *Solar Energy Materials and Solar Cells* 2009; **93**: 825–830.
4. Young DL, Pinegar S, Stradins P. New Real-Time Qauntum Efficiency Measurement System. *33rd IEEE Photovoltaic Specialists Conference*, San Diego, California, 11–16 May, 2008.

5. Riede MK, Mueller T, Maennig B, Leo K, Sylvester-Hvid KO, Zimmermann B, Niggemann M, Gombert A. Comment on 'roles of donor and acceptor nanodomains in 6% efficient thermally annealed polymer photovoltaics' [appl. phys. lett. 90, 163511 (2007)]. *Applied Physics Letters* 2008; **92**(7): 18.
6. Dennler G. The value of values. *Materials Today* 2007; **10**(11): 56–56.
7. Gilot J, Wienk MM, Janssen RAJ. On the efficiency of polymer solar cells. *Nature Materials* 2007; **6**(10): 704.
8. Smestad GP, Krebs FC, Lampert CM, Granqvist CG, Chopra KL, Mathew X, Takakura H. Reporting solar cell efficiencies in solar energy materials and solar cells. *Solar Energy Materials and Solar Cells* 2008; **92**(4): 371–373.
9. Cárabe J. A new approach to measuring spectral responses of nonlinear solar cells. *Solar Cells* 1991; **31**(1): 39-L 46;
10. Bucher K, Schonecker A. Spectral response measurements of multi-junction solar cells with a grating monochromator and a Fourier spectrometer. *Proceedings of the 10th European Photovoltaic Solar Energy Conference*, Lisbon, 1991; 107- 110.
11. Glatthaar M, Niggemann M, Zimmermann B, Lewer P, Riede M, Hinsch A, Luther J. Organic solar cells using inverted layer sequence. *Thin Solid Films* 2005; **491**(1–2): 298–300.
12. Zimmermann B, Glatthaar M, Niggemann M, Riede MK, Hinsch A, Gombert A. Ito-free wrap through organic solar cells—a module concept for cost-efficient reel-to-reel production. *Solar Energy Materials and Solar Cells* 2007; **91**(5): 374–378.
13. Jørgensen M, Norrman K, Krebs FC. Stability/degradation of polymer solar cells. *Solar Energy Materials and Solar Cells* 2008; **92**: 686–714.
14. National Renewable Energy Laboratory (NREL), MS Excel™ spreadsheet file downloaded from http://rredc.nrel.gov/solar/spectra/am1.5/
15. Data sheet for Hamamatsu photo-diode: S5971, S5972 and S5973 series.
16. Chirvase D, Chiguvare Z, Knipper M, Parisi J, Dyakonov V, Hummelen JC. Temperature dependent characteristics of poly(3 hexylthiophene)-fullerene based heterojunction organic solar cells. *Journal of Applied Physics* 2003; **93**(6): 3376–3383;
17. Krebs FC, Gevorgyan SA, Gholamkhass B, Holdcroft S, Schlenker C, Thompson ME, Thompson BC, Olson D, Ginley DS, Shaheen SE, Alshareef HN, Murphy JW, Youngblood WJ, Heston NC, Reynolds JR, Jia S, Laird D, Tuladhar SM, Dane JGA, Atienzar P, Nelson J, Kroon JM, Wienk MM, Janssen RAJ, Tvingstedt K, Zhang F, Andersson M, Inganäs O, Lira-Cantu M, de Bettignies R, Guillerez S, Aernouts T, Cheyns D, Lutsen L, Zimmermann B, Würfel U, Niggemann M, Schleiermacher H-F, Liska P, Grätzel M, Lianos P, Katz EA, Lohwasser W, Jannon B. A round robin study of flexible large-area roll-to-roll processed polymer solar cell modules. *Solar Energy Material and Solar Cells* 2009; **93**: 1968-L 1977.
18. Shrotriya V, Li G, Yao Y, Moriarty T, Emery K, Yang. Y. Accurate measurement and characterization of organic solar cells. *Advanced Functional Materials* 2006; **16**: 2016–2023.
19. Pysch D, Mette A, Glunz SW. A review and comparison of different methods to determine the series resistance of solar cells. *Solar Energy Materials and Solar Cells* 2007; **91**: 1698–1707.
20. Mihailetchi VD, Wildeman J, Blom. PWM. Space-charge limited photocurrent. *Physical Review Letters* 2005; **94**(12): 126602.
21. Mihailetchi VD, Xie HX, de Boer B, Koster LJA, Blom. PWM. Charge transport and photocurrent generation in poly(3-hexylthiophene): methanofullerene bulk-heterojunction solar cells. *Advanced Functional Materials* 2006; **16**(5): 699–708.
22. Dyakonov V. Mechanisms controlling the efficiency of polymer solar cells. *Applied Physics A: Materials Science & Processing* 2004; **79**(1): 21–25.
23. Koster LJA, Mihailetchi VD, Xie H, Blom. PWM. Origin of the light intensity dependence of the short-circuit current of polymer/fullerene solar cells. *Applied Physics Letters* 2005; **87**(20): 203502.
24. Chirvase D, Chiguvare Z, Knipper M, Parisi J, Dyakonov V, Hummelen JC. Electrical and optical design and characterisation of regioregular poly(3-hexylthiophene-2,5diyl)/fullerene-based heterojunction polymer solar cells. *Synthetic Metals* 2003; **138**(1–2): 299–304.
25. Chirvase D, Parisi J, Hummelen JC, Dyakonov V. Influence of nanomorphology on the photovoltaic action of polymer-fullerene composites. *Nanotechnology* 2004; **15**(9): 1317–1323.
26. Dennler G, Forberich K, Scharber MC, Brabec CJ, Tomis I, Hingerl K, Fromherz T. Angle dependence of external and internal quantum efficiencies in bulk-heterojunction organic solar cells. *Journal of Applied Physics* 2007; **102**(5): 054516.
27. Jin S-H, Naidu BVK, Jeon H-S, Park S-M, Park J-S, Kim SC, Lee JW, Gal. Y-S. Optimization of process parameters for high-efficiency polymer photovoltaic devices based on P3HT:PCBM system. *Solar Energy Materials and Solar Cells* 2007; **91**(13): 1187–1193.
28. Kim Y, Choulis SA, Nelson J, Bradley DDC, Cook S, Durrant JR. Composition and annealing effects in polythiophene/fullerene solar cells. *Journal of Material Science* 2005; **40**(6): 1371–1376.
29. Kim Y, Choulis SA, Nelson J, Bradley DDC, Cook S, Durrant JR. Device annealing effect in organic solar cells with blends of regioregular poly(3-hexylthiophene) and soluble fullerene. *Applied Physics Letters* 2005; **86**(6): 063502.
30. Kim Y, Cook S, Tuladhar SM, Choulis SA, Nelson J, Durrant JR, Bradley DDC, Giles M, McCulloch I,

Ha C-S, Ree. M. A strong regioregularity effect in self-organizing conjugated polymer films and high-efficiency polythiophene:fullerene solar cells. *Nature Materials* 2006; **5**(3): 197–203.
31. Moule AJ, Meerholz K. Intensity-dependent photocurrent generation at the anode in bulk-heterojunction solar cells. *Applied Physics B—Lasers and Optics* 2008; **92**(2): 209–218.
32. Padinger F, Rittberger RS, Sariciftci NS. Effects of postproduction treatment on plastic solar cells. *Advanced Functional Materials* 2003; **13**(1): 85–88.
33. Riedel I, Dyakonov V. Influence of electronic transport properties of polymer-fullerene blends on the performance of bulk heterojunction photovoltaic devices. *Physica Status Solidi A: Applied Research* 2004; **201**(6): 1332–1341.